ROYAL SOCIETY
OF CHEMISTRY

PAPER

CrossMark
← click for updates

Study on advanced Ce$_{0.9}$La$_{0.1}$O$_2$/Gd$_2$Zr$_2$O$_7$ buffer layers architecture towards all chemical solution processed coated conductors

Y. Zhao,*[a] L. Ma,[ab] W. Wu,[ac] H.-L. Suo[b] and J.-C. Grivel[a]

Chemical solution deposition is a versatile technique to deposit functional oxide films with low cost. In this study, this approach was employed to grow multi-layered, second-generation, high-temperature superconductors ("coated conductors") with high superconducting properties. The Ce$_{0.9}$La$_{0.1}$O$_2$/ Gd$_2$Zr$_2$O$_7$ buffer layer stack and the 200 nm thick YBa$_2$Cu$_3$O$_7$ (YBCO) superconducting layer were sequentially deposited on textured NiW substrates using metal–organic deposition routes. The surface texture of the Gd$_2$Zr$_2$O$_7$ barrier layer deteriorates when the film thickness increases to 80 nm, although the global texture retains a sharp biaxial orientation, as determined by conventional X-ray diffraction. We paid particular attention to improving the surface quality in terms of crystallographic orientation and local flatness after depositing a Ce$_{0.9}$La$_{0.1}$O$_2$ thin film as a cap layer. From a comprehensive analysis of the surface morphology and misorientation maps constructed by electron backscattering diffraction, it is found that these improvements are mainly attributed to: (i) the preferential nucleation of Ce$_{0.9}$La$_{0.1}$O$_2$ crystals on the Gd$_2$Zr$_2$O$_7$ grains with desirable orientations; and (ii) the predominant two-dimensional growth of the Ce$_{0.9}$La$_{0.1}$O$_2$ crystals in the layer. Moreover, the microstructure and superconducting performance of the YBCO superconducting layer were thoroughly characterized and compared with those of films deposited on single-crystal substrates using the same technique. A promising critical current density of 2.2 MA cm^{-2} (77 K, self-field) was achieved on such an all chemical derived configuration, demonstrating the high quality of the buffer layer stack and the feasibility of using all chemical solution routes for the fabrication of low-cost coated conductors.

Introduction

The rapid development of second-generation high-temperature superconductors (2G HTS, YBCO-based coated conductors) in terms of superconducting performance and industrialization level holds promise for a revolution in emerging energy applications. The main challenges in material science focus on further improvements in the performance of the coated conductors through low-cost routes. To realize the epitaxial multi-layer architecture in 2G HTS tapes, both physical and chemical film deposition techniques have been investigated and employed in the fabrication processes worldwide. To date, the physical deposition approaches adopted by most groups/ companies have yielded superior superconducting performance[1–3] because of their well-established protocols and rigorous growth conditions (such as high-vacuum and limited

growth rate). On the other hand, chemical solution deposition (CSD) processes, which can operate under normal or low-vacuum conditions, have received less attention.[4] From an economic point of view, however, chemical deposition routes could reach lower price targets considering the lower capital investments and relatively high growth rates of the films using these methods. In order to make CSD routes competitive with physical deposition approaches, more and more recent efforts have focused on further understanding the fundamental issues involved in CSD routes, including coating techniques,[5] solution chemistry,[6,7] and film nucleation and growth.[8,9] However, comprehensive knowledge is still far away from being achieved.

In the all-CSD routes used to manufacture coated conductors, the biaxial orientation of the oxide films (both buffer layers and superconducting layers) is transferred from highly textured Ni-based tapes. Additionally, the cap layer (defined as the buffer layer close to the superconducting layer) plays an essential role in the nucleation of the YBCO layer and consequently has a strong influence on its superconducting performance. Compared to the microstructural characteristics (lattice mismatch, roughness and texture), several key surface properties including termination, polarity and catalytic activity remain poorly explored for cap layers.[10] Thus far, the best candidates for

[a]*Department of Energy Conversion and Storage, Technical University of Denmark, Frederiksborgvej 399, DK-4000 Roskilde, Denmark. E-mail: zhyu@dtu.dk*

[b]*College of Materials Science and Engineering, Beijing University of Technology, 100124 Beijing, China*

[c]*Department of Electrical Engineering, Shanghai JiaoTong University, 200240 Shanghai, China*

a cap layer deposited by chemical routes are cerium oxide-based materials, which possess high melting temperatures ($\sim$2500 °C) and stable cubic fcc (fluorite) structures.[11] To date, cerium films with various dopants have been investigated in view of further enhancing/multi-functionalizing the cap layer performance. Recently, we proposed and developed La-doped CeO_2 ($Ce_{0.9}La_{0.1}O_2$, CLO) as a cap layer for an all chemical-derived coated conductor configuration.[12] A YBCO layer grown on a CLO-buffered yttrium-stabilized ZrO_2 (YSZ) template exhibited high performance (>3 MA cm^{-2}) comparable to that of films grown on single-crystalline $LaAlO_3$ by a low-fluorine metallic organic deposition route.[13] Compared with pure CeO_2, the main advantages of CLO as a cap layer are: almost perfect lattice match with YBCO; and superior surface properties resulting from the high grain boundary mobility due to the La^{3+} dopant. It is believed that both would be beneficial for the nucleation and growth of YBCO layers.

In this work, as a further step toward enhancing the understanding of the key factors in the development of all chemical solution coated conductors, CLO is employed as a cap layer on a $Gd_2Zr_2O_7$ (GZO)/NiW technical template, where GZO serves as barrier layer against diffusion between the YBCO film and the metallic substrate. The surface properties of the CLO cap layer with respect to the GZO/NiW templates are thoughtfully characterized by means of electron backscattering diffraction (EBSD) and scanning electron microscopy (SEM). The improvement in surface quality after depositing the CLO cap layer is discussed based on a self-epitaxy mechanism. Eventually, a full coated conductor structure with an YBCO/CLO/GZO/NiW constitution was achieved *via* an all chemical solution deposition route to assess the compatibility of the films in a complete multi-layer structure.

Experimental

Synthetic procedures

The textured Ni5W alloy substrates used in this study were purchased from Evico GmbH. Prior to coating, the substrates were annealed in 5% H_2/N_2 flowing gas at 850 °C for 20 min followed by cleaning in ultrasonic ethanol for 5 min and compressed air drying. GZO layers were deposited by using a propionate-based metal–organic solution with a fixed total cation concentration of 0.4 mol L^{-1}. The dip-coating technique was used to prepare the films under ambient conditions. After immersing the substrate into the precursor, withdrawal speeds in the range of 20–40 mm min^{-1} were applied. The coated films were dried in air for several minutes and directly inserted into an alumina tube furnace for crystallization, as reported previously.[14,15] Additionally, a multiple coating procedure was used to increase the film thickness, *i.e.*, the coating and annealing processes were repeated two or three times.

The precursor solution used to coat the CLO layer was synthesized by dissolving stoichiometric amounts of the reagents, cerium(III) and lanthanum(III) 2,4-pentadionates (both from Aldrich), in propionic acid at 150 °C until the color of the solution changed from light yellow to dark brown. The total cation concentration of the precursor was fixed at 0.2 mol L^{-1}.

The substrate cleaning, solution coating and annealing were applied to obtain CLO cap layers similar to the GZO layer. The annealing atmosphere for both the GZO and CLO layers was 5% H_2/N_2 forming gas.

To assess the quality of the CLO/GZO/NiW buffer layer stack, a 200 nm thick YBCO layer was deposited by the low-fluorine (LF-) metal–organic deposition route.[13] In this LF-solution, only stoichiometric amounts of the yttrium and barium sources react with TFA, while a fluorine-free copper salt is synthesized by dissolving copper acetate in excess acrylic acid. After mixing and rotary evaporation, the total cation concentration was adjusted to 1.5 mol L^{-1} by adding methanol. The precursor was spin-coated on a 5 mm × 5 mm buffered substrate. The heat-treatment procedure including pyrolysis, crystallization and oxygenation were performed as reported previously on the single-crystal substrates. For comparison, the YBCO films were also deposited on CLO/YSZ and $LaAlO_3$ single-crystal substrates under similar conditions.

Structural and superconductivity characterization

The phases and textures of the films were investigated using a four-circle diffractometer (Bruker D8) with Cu Kα radiation. EBSD measurements were carried out using a scanning electron microscope (Zeiss Supra 35) equipped with a detector from HKL Technology. The surface textures of the CLO and GZO layers without any post-treatment were characterized by EBSD in an area of about 430 × 390 μm^2 under normal operating conditions (electron energy of 15 kV in high-current mode). The Kikuchi patterns were automatically analyzed by the data handling software package (Channel 5). To evaluate the surface texture quality, the indexing rate on the sample surface was extracted from the EBSD mapping without any *noise reduction* operation. The surface morphologies of the films was evaluated using the same scanning electron microscope with an in-lens detector. Atomic force microscopy (AFM; DualScope DME Danish Micro Engineering A/S, Denmark) using a silicon tip was employed to evaluate the surface roughness. The superconducting transition temperature (T_c) was determined by resistance–temperature measurements in a Quantum Design Physical Property Measurement System (PPMS®) using the four-point method. The critical current densities, J_c, were calculated based on the Bean model using the opening of the hysteresis loops measured by a vibrating sample magnetometer (VSM, CRYOGENIC cryogen free measuring system) under a magnetic field applied perpendicular to the plane of the films.

Results and discussion

Thickness dependence of texture quality in the $Gd_2Zr_2O_7$/NiW template

In order to guarantee the sufficient barrier function of the buffer layer used in coated conductors, barrier layers of a certain thickness are needed. Additionally, the microstructure of the barrier plays an essential role in preventing the diffusion of metal elements from the substrate. Defects such as cracks, voids and grain boundaries can act as shortcuts for element

13276 | *J. Mater. Chem. A*, 2015, **3**, 13275–13282

This journal is © The Royal Society of Chemistry 2015

diffusion at high temperatures.[16] Although the precursors, films thicknesses and annealing procedures are the key factors in determining the texture quality of the CSD-buffer layer, there are seemingly no significant microstructural differences among rare-earth zirconate layers, especially for the thick films prepared by mono-coating routes. Similar sponge-like microstructures with high densities of nanovoids have been observed by several groups in the film bodies as well as on the surfaces of the CSD buffer layers[14,17–20] despite the use of varying materials, solution synthetic routes and heat treatment processes. To date, no direct evidence has been found to explain the formation of such structural features. It is, nevertheless, believed that porosity is related to the gas release during the early stage of heat treatment when metal–organic precursors start decomposing into crystalline or amorphous oxides. In previous works, we obtained a nanovoid-free structure in a 20 nm thick, highly textured GZO film, indicating a strong correlation between the microstructure and the thickness of the film prepared by a mono-coating process.[21] In this study, to obtain a similar microstructure (*i.e.*, void-free or low-porosity) in thick GZO barrier layers, a multi-coating route is employed rather than increasing the thickness in a mono-coated film. First, the thickness dependence of the texture quality in the GZO/NiW template was quantitatively investigated by X-ray diffraction (XRD) and EBSD (Fig. 1). We noticed similar trends in *c*-axis orientation extracted from the XRD θ–2θ scans and the in-plane texture quality determined by the (222) GZO phi-scans with increasing film thickness, indicating a sharp texture on all the GZO films up to a thickness of 80 nm. Apparently, a small drop in the *c*-axis orientation percentage in the 80 nm thick GZO film results from the presence of the low-intensity GZO (222) reflection. This undesirable GZO (222) reflection was also discerned by an XRD area-detector in our previous study, where two textural components (*i.e.*, a sharp <220> (004) texture and a random orientation) coexist in the films.

Overall, the difference in global texture between the 80 nm thick and the thinner GZO films is minor. However, thickness is significant for surface crystallization as illustrated in the EBSD

maps collected on the sample surfaces of two representative films with thicknesses of 60 and 80 nm (Fig. 2). Both misorientation maps show similar granular structures indicative of the transferring of texture from the underlying NiW substrates. The indexing rate of the 60 nm thick GZO film is as high as 98.5%, with most of the area within the individual NiW grains being well indexed (*i.e.*, most of the un-indexed points are located along the grain boundaries of the NiW substrate beneath and on some large surface contaminations indicated by short arrows in the figures). In contrast, the 80 nm thick GZO film only yields an indexing rate of 78% in this selected area,
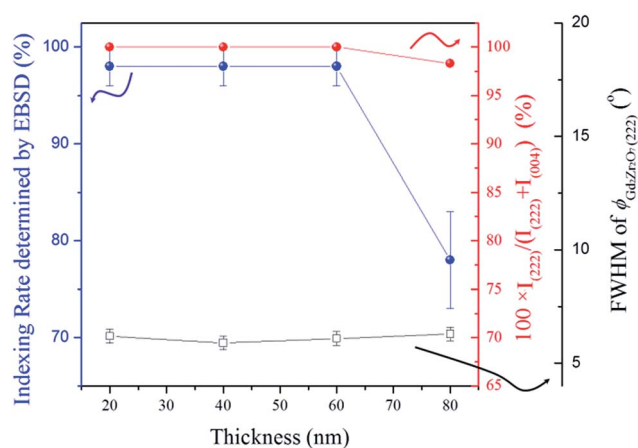

Fig. 2 Misorientation maps acquired from the 60 nm- and 80 nm-thick Gd$_2$Zr$_2$O$_7$ layers (upper and lower). The inset is the Gd$_2$Zr$_2$O$_7$ (222) XRD pole-figure calculated from this region. The highlighted colors (from blue to red in the color bar) represent tolerance angles deviating from the ideal orientation in degree. Zero solution points are represented in white and indicated by arrows (short arrows for grain boundaries, particles and twin grains inherited from the substrate, and long arrows for the unsolved points within individual NiW grains). The scale bars for both maps are 100 μm. Note that for comparison, *noise-reduction was not performed*.

Fig. 1 Thickness dependence of the global and surface textures of the Gd$_2$Zr$_2$O$_7$ layers determined by conventional XRD and EBSD techniques.
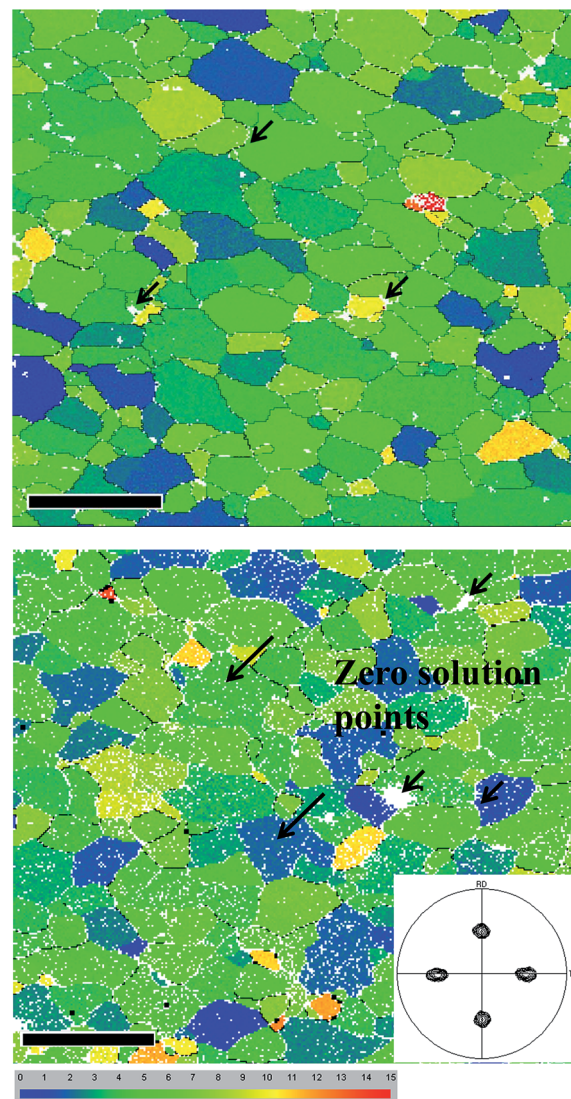
This journal is © The Royal Society of Chemistry 2015

J. Mater. Chem. A, 2015, **3**, 13275–13282 | **13277**

while the GZO (222) pole-figure shown as an inset demonstrates the highly biaxial texture of these indexed regions.

All the layers discussed in this paper exhibit similar roughness values (*i.e.*, rms values in the range of 2 to 5 nm on each individual NiW grain) comparable to those of NiW substrates. Therefore, the surface roughness has little influence on the quality of the Kikuchi patterns in this case. A closer examination of this second map reveals that a large amount of the un-indexed points are randomly distributed within the individual underlying NiW grains. Given that the grain size of the NiW substrate is larger than that of the GZO films by several orders of magnitude, the nano-sized GZO particles on individual NiW grains are expected to nucleate and grow in exactly the same conditions. The influence of the substrate texture and morphology is therefore very limited. The main reason for these un-indexed points is the poor local texture quality on the sample surface. According to Monte Carlo simulations,[22,23] the lateral resolution of the EBSD technique is on the order of 50 to 100 nm depending on the operating conditions (current, voltage, *etc.*). Thus, each Kikuchi pattern obtained on the present GZO films includes information integrated in an area consisting of several GZO grains. As a consequence, only when the entire region (several GZO nano-grains) illuminated by the electron beam exhibits a single textural component will a clear Kikuchi pattern appear and be subsequently indexed by the program. In fact, it is not surprising to find a relatively poor textures on the surfaces of thicker films. When the film thickness is increased by applying a multi-coating route, there is the probability of introducing defects to the interface. The inhomogeneous release of residual carbon, which is the essential issue for obtaining highly epitaxial films grown by chemical solution methods, may also be involved.

Growth of a $Ce_{0.9}La_{0.1}O_2$ cap layer on top of a thick GZO barrier layer

A 20 nm thick CLO cap layer was deposited on an 80 nm thick GZO layer in order to investigate the improvement of the surface quality. The surface morphology before and after CLO cap layer deposition was observed by SEM, as shown in Fig. 3. As expected, the 80 nm thick GZO layer is rather dense and consists of equiaxed grains with a dome top. The lateral grain size (G.S.) is in the range of 10 to 40 nm. The image contrast in the local region also reveals the height differences in the sample surface, *i.e.*, the dark regions are relatively deeper than the bright ones (more visible in the inset of the Fig. 3). On the contrary, the CLO layer exhibits a quite different surface morphology in terms of flatness, grain geometry, and lateral G.S. (around 100 nm). It can be seen that the entire surface is covered by square-shaped grains with atomically flat tops, except for a small portion of nanosized pores at grain boundaries.

Combined with the crystallographic orientation analysis, it can also be deduced that the top of the CLO crystal is CLO (002), which is parallel to the normal direction of the NiW substrate (NiW (002)). In contrast, the edges of the CLO crystals are CLO <220>, *i.e.*, parallel to the transverse/rolling direction of the NiW substrate (NiW <001>). The coherence between the

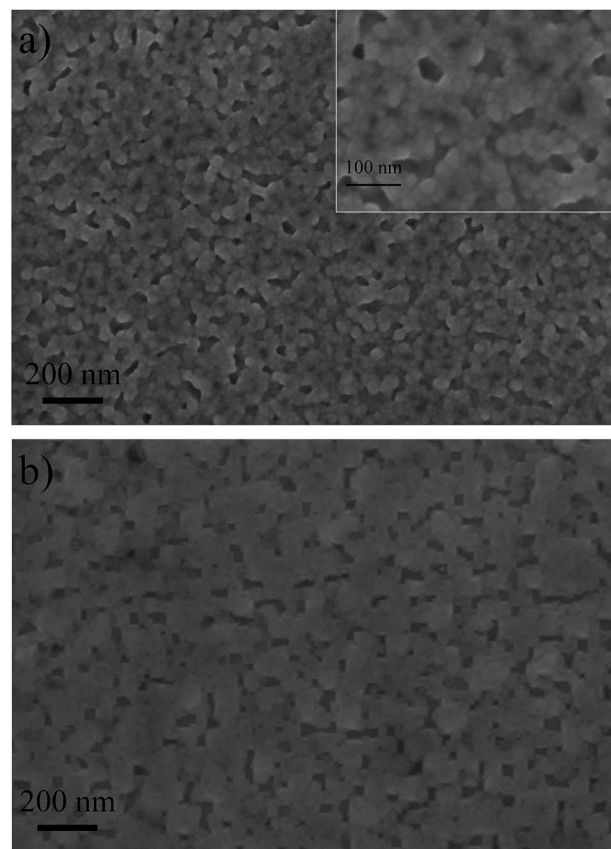**Fig. 3** SEM images of the 80 nm thick $Gd_2Zr_2O_7$ layer before (a) and after (b) depositing the $Ce_{0.9}La_{0.1}O_2$ cap layer.

crystallographic orientation and the geometrical alignment are indicative of a high biaxial texture quality in the CLO deposited on top of the GZO/NiW template. Moreover, the local flatness of the buffer layer stack is significantly improved, as evidenced by the reduction in the portion of the dark region from 26% to 8% after the deposition of the CLO layer.

Additionally, the surface texture of the CLO layer is also confirmed by EBSD (Fig. 4). The indexing rate in this layer reaches 98.5%, which is 20% higher than that of the GZO layer. The uniform colors within the area defined by the underlying individual NiW grains suggest that the un-indexed regions were perfectly covered by CLO crystals with sharp textures.

To shed light on this surface improvement behavior, both nucleation and growth characteristics are taken into consideration. First, it was found that the grains with good texture quality generally have larger crystallite size and consequently less strain, which would be energetically favorable for the nucleation of the layer on the top.[24] Textural improvements have been observed in several multilayer stacks such as CeO_2 on IBAD–GZO substrates,[25] and YBCO on LMO/epi-MgO/IBAD–MgO substrates.[26] A similar mechanism probably also drives the nucleation of the CLO grown on the GZO layer, *i.e.*, CLO crystals preferably nucleate at GZO grains with sharp textures due to the minimization of interfacial energy. Secondly, CeO_2-based thin films with atomically-flat surfaces were observed on both single-
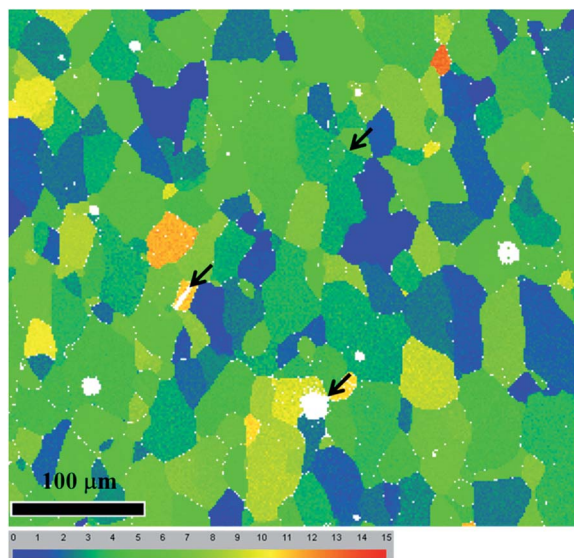
13278 | *J. Mater. Chem. A*, 2015, **3**, 13275–13282

This journal is © The Royal Society of Chemistry 2015

Fig. 4 Misorientation map acquired from the $Ce_{0.9}La_{0.1}O_2$ cap layer grown on an 80 nm thick $Gd_2Zr_2O_7$ layer.

crystal and metallic substrates; the formation of these films is governed by several certain critical conditions such as thickness and annealing temperature.[27,28] It is also worth noting that in both cases, another prominent feature associated with this morphology is the two-dimensional growth mode, as demonstrated by a much larger lateral grain size with respect to the thickness. This is one of the most essential prerequisites for improving the poor surface texture and smoothness of the thick GZO layer in this study. Based on the classical grain-growth models of polycrystalline films, a grain with a favored orientation has growth advantages; that is, grains with favorable orientations grow at the expense of those with less-favored orientations. Taking advantage of the preferential nucleation and growth, the biaxially oriented CLO nuclei are higher in density and are subsequently able to further develop mainly within the plane; they thus cover the GZO regions, even with poor biaxial texture.

A schematic summary of the growth process of the CLO cap layer responsible for the surface improvement is proposed and

shown in Fig. 5. In the GZO/NiW templates, the local surface quality in terms of texture and flatness is not optimal. After the deposition of a CLO layer, the nuclei form with preferential orientations; that is, nucleation favorably occurs at interfaces with the GZO <220> (004) orientation, while the nucleation density would be much lower on surfaces with other orientations. Consequently, a larger amount of CLO nuclei with the desirable textural component CLO <110> (002) is able to further develop and cover most of the film surface by consuming the amorphous precursor or the smaller crystals forming on the top of the poorly textured GZO grains, *i.e.*, the two-dimensional growth mode.

Structural and superconducting properties of the YBCO layers

First, the XRD θ–2θ scan, YBCO (103) pole-figure, (005) rocking curve and (103) phi-scan were routinely performed in order to obtain global structural information on the YBCO layer deposited on the all chemical buffered NiW substrate. As shown in Fig. 6a, strong YBCO (00l) peaks with minor secondary diffractions can be seen, indicating a sharp *c*-axis orientation. The presence of some impurities, $BaCeO_3$ (almost randomly orientated) and $NiWO_4$ (partly textured), also indicate the inevitable interactions between YBCO and the buffered substrate, even at low growth temperature (740 °C). Only four-fold concentrated poles in the YBCO (103) XRD pole-figure (Fig. 6b) confirm the high quality of the in-plane and out-of-plane textures. The average FWHM values of the YBCO (005) rocking curve and the YBCO (103) phi-scan are 5.1° and 7.5°, respectively, which are comparable with the corresponding values for the buffer layers. These results imply that the formation of these secondary phases most likely occurs after the nucleation of YBCO. The YBCO nuclei with high degrees of biaxial texture are seemingly able to develop further by consuming the intermediate phases, while the YBCO formed at the interface simultaneously reacts with the cap layer during the dwell stage. The morphology of the film observed by SEM is shown in Fig. 7. Generally, the film is homogeneous, smooth and almost featureless. No distinguishable grain boundary with the underlying NiW substrate is visible, demonstrating the planarization of the metallic substrate after the deposition of the buffer layer stack. From the high-magnification SEM picture, it is clearly seen that the plate-
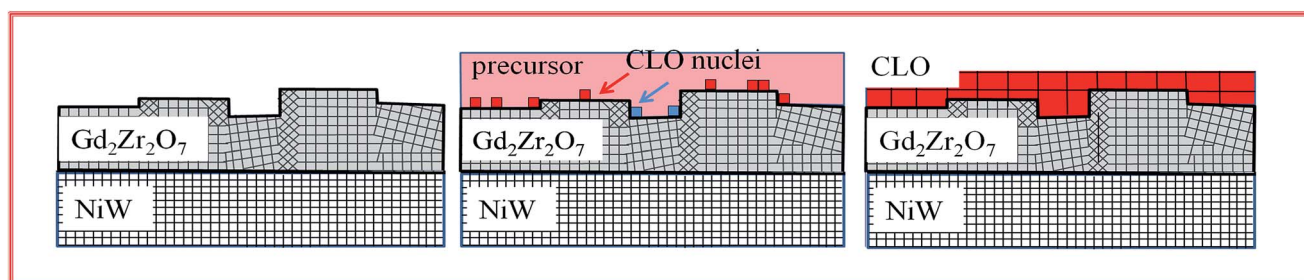

Fig. 5 Schematic of the nucleation and growth processes of the $Ce_{0.9}La_{0.1}O_2$ cap layer on the $Gd_2Zr_2O_7$ layer. For simplification, both the GZO and CLO layers grown on an individual NiW grain are taken into consideration. The grids with different tilted angles represent the crystallographic orientations of the NiW substrate, the GZO layer and the CLO layer. The red squares represent the CLO nuclei with favored epitaxial orientations, while the blue squares represent those with less epitaxial or random orientations.
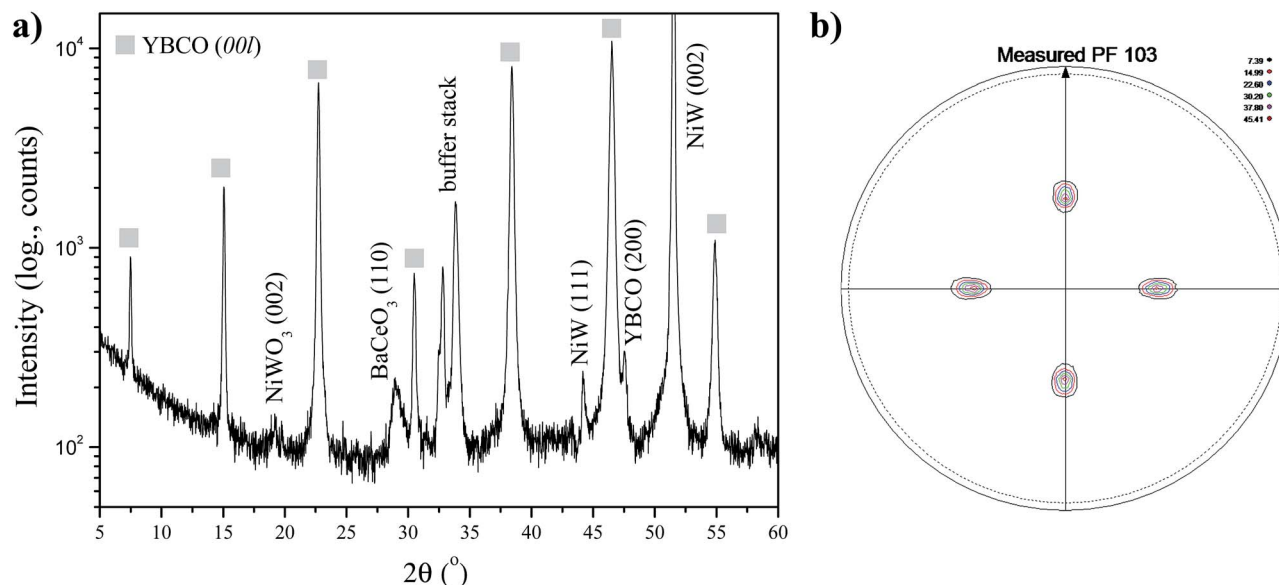
Fig. 6 Conventional XRD analysis of a fully structured YBCO/$Ce_{0.9}La_{0.1}O_2$/$Gd_2Zr_2O_7$/NiW stack: (a) $\theta-2\theta$ scan and (b) YBCO (103) pole-figure.
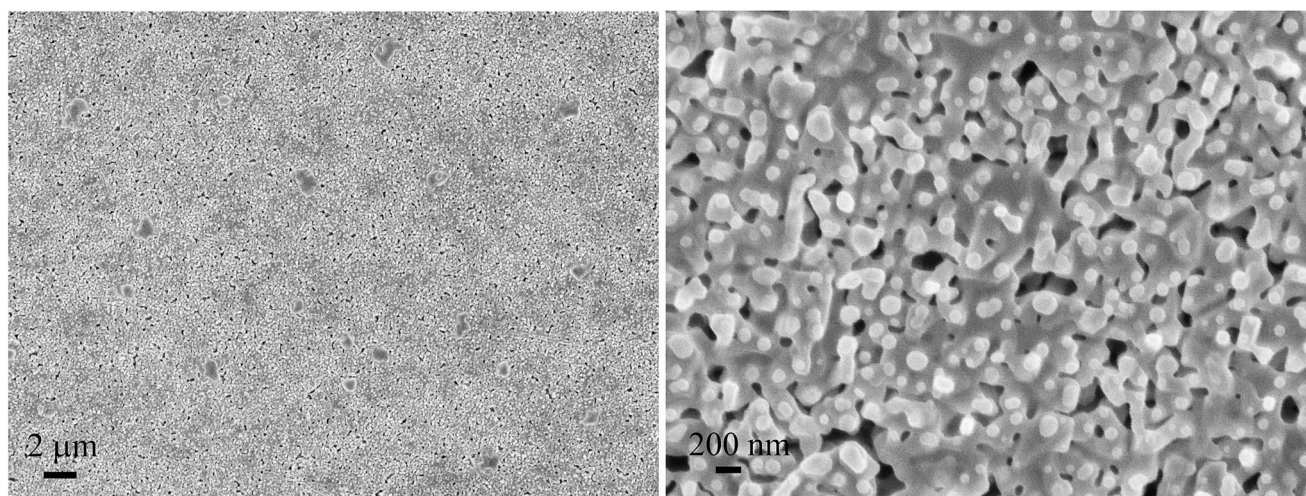

Fig. 7 SEM images of the surface of a fully structured YBCO/$Ce_{0.9}La_{0.1}O_2$/$Gd_2Zr_2O_7$/NiW.

like YBCO grains are larger than 200 nm in diameter. In addition, it can be noticed that the microstructure is inhomogeneous on the sub-micrometer scale (*i.e.*, dense and porous regions coexist). A similar feature was also observed in MOD–YBCO films deposited on either a buffered single crystal (CLO/YSZ) or a LaAlO$_3$ single crystal in a similar temperature range.[13] It is therefore believed that such a structure is probably connected with the coarsening behavior resulting from the limited atomic mobility at relatively low growth temperatures.

The temperature dependence of the normalized resistance (R–T plot) was obtained by the four-point contact technique on the YBCO layer deposited on the all chemical buffered substrate (Fig. 8a). The superconducting transition occurs between 86 and 90 K, with a transition width ΔT_c of about 2.7 K (inset of Fig. 8a). The high resistance ratio of R (285 K)/(100 K) $\geq$ 2.5 and

linear resistance that extrapolates nearly to zero at 0 K in the R–T plot are typical features of high-quality YBCO films with little grain boundary scattering in the normal state.[29] The $J_c(B)$ of the YBCO film at 77 K was calculated from the hysteresis loops measured by VSM and is shown in Fig. 8b. For comparison, the $J_c(B)$ values of YBCO films grown on a buffered single crystal (CLO/YSZ) and on an LaAlO$_3$ single crystal are also plotted in Fig. 8b. On the double-log scale, similar $J_c(B)$ behaviors were observed for all three YBCO films (*i.e.*, three regions including a plateau at low fields (up to the accommodation field, B^*), a power-law dependence $J_c(B)$ and a high-field limit where J_c decreases rapidly). We noticed a small hump (indicated by an arrow) at around 200 mT for the YBCO film grown on the technical substrate, which is absent in the curves for YBCO grown on the two single crystals. This anomaly could be

13280 | *J. Mater. Chem. A*, 2015, **3**, 13275–13282

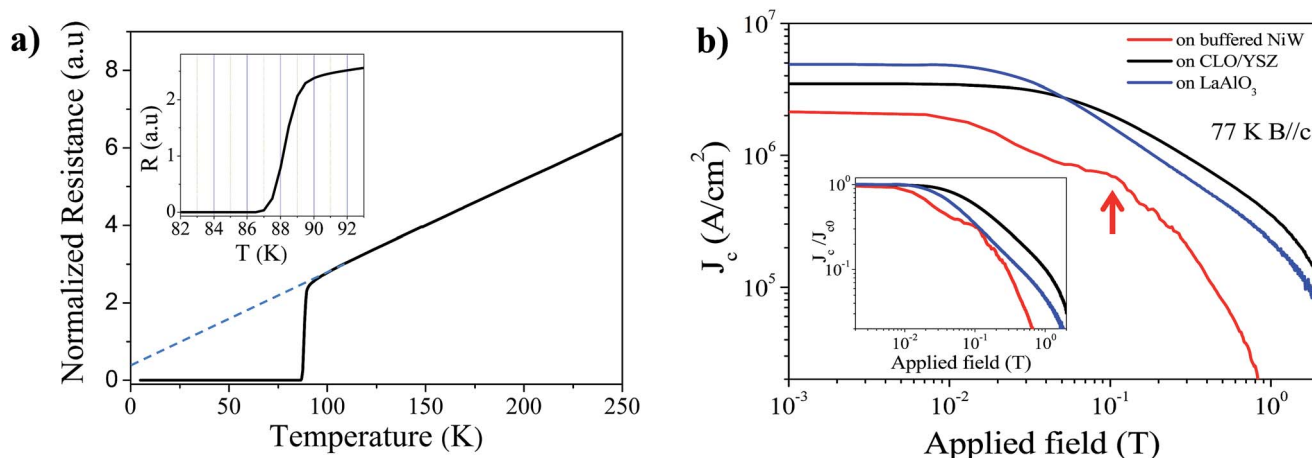This journal is © The Royal Society of Chemistry 2015

Fig. 8 (a) Four-probe transport measurement of the temperature dependence of the normalized resistance. The dashed line shows the extrapolation of the linear temperature part of the resistance line to low temperatures, and the inset is the magnification of the transition. (b) Double logarithmic plots of J_c vs. magnetic field B measured at 77 K for the YBCO/Ce$_{0.9}$La$_{0.1}$O$_2$/Gd$_2$Zr$_2$O$_7$/NiW stack and the reference samples (grown on the CLO/YSZ single crystal at 740 °C and grown on an LaAlO$_3$ single crystal at 800 °C). Inset: J_c vs. magnetic field normalized with J_c at self-field.

associated with a grain boundary effect or with a second type of field-activated pinning centers attributed to oxygen defects.[30,31] It is worth pointing out that the J_c value of the YBCO film grown by the all-chemical route reaches 2.2 MA cm^{-2}, which is promising compared to those of films grown on similar substrates by vacuum physical deposition techniques.[12,32] The relatively lower J_c value of the YBCO film on the technical substrate compared to the films on single crystals is due to grain-boundary limitations. Finally, the normalized $J_c(B)$ dependence at 77 K was plotted and shown in the inset of Fig. 8b. A smaller B^* and sharper drop-off of $J_c(B)$ at higher external fields ($>B^*$) for the film grown on the technical substrate are also discerned; these are most likely due to the presence of low-angle grain boundaries in the YBCO films inherited from the NiW substrate underneath.[33]

Conclusions

In this paper, we investigated the role of CLO films as cap layers in YBCO/CLO/GZO/NiW coated conductors fabricated by all chemical solution routes. The thickness dependence of the GZO layers deposited by a multi-coating approach shows that the surface texture deteriorates when the film thickness increases up to 80 nm, although the global texture determined by conventional XRD exhibits a sharp biaxial orientation comparable with those of thinner films. Most interestingly, a significant improvement in the surface quality in terms of flatness and crystallographic orientation is observed after depositing CLO films on top of the 80 nm thick GZO template. The square-shaped CLO crystals with flat tops fully cover the granular GZO grains with dome-like tops. By checking the EBSD misorientation maps, the indexing rate of the Kikuchi patterns increases from 78% to 98.5% after CLO layer deposition, which is a clear indication of the enhancement of the desirable texture on the surface.

Nucleation with preferential orientation occurring on textured GZO regions and the predominant two-dimensional growth of the CLO layer are two main reasons for this improvement in surface quality. Finally, a YBCO film was grown on the buffer layer stack by a low-fluorine metal–organic decomposition route. Compared with films deposited on CLO-buffered YSZ and blank LaAlO$_3$ single crystals, a promising J_c value of 2.2 MA cm^{-2} was obtained by this all chemical solution processed coated conductor structure. This study suggests the essential role of using this type of CLO films as a cap layer and demonstrates the feasibility of growing high-quality coated conductor structures with low-cost chemical-solution routes.

Notes and references

1 A. Usoskin, T. Bubelis and A. Rutt, *et.al.*, Long-length YBCO coated conductors manufactured in medium size pilot production line based on pulsed laser deposition, *ICEC/ICMC Conference*, 2014.

2 Y. Shiohara, T. Taneda and M. Yoshizumi, *Jpn. J. Appl. Phys.*, 2012, **51**, 010007.

3 D. W. Hazelton and V. Selvamanickam, *Proc. IEEE*, 2009, **97**, 1831–1836.

4 M. Bäcker, Recent Progress in Development of All-Solution Coated Conductors at Deutsche Nanoschicht, *Applied superconductivity conference*, 2013.

5 M. Vilardell, X. Granados and S. Ricart, *et.al.*, *Thin Solid Films*, 2013, **548**, 489–497.

6 G. Pollefeyt, S. Clerick and P. Vermeir, *et.al.*, *Inorg. Chem.*, 2014, **53**, 4913–4921.

7 M. Erbe, J. Hanisch and T. Freudenberg, *et.al.*, *J. Mater. Chem. A*, 2014, **2**, 4932–4944.

8 X. Obradors, T. Puig and M. Gibert, *et.al.*, *Chem. Soc. Rev.*, 2014, **43**, 2200–2225.

This journal is © The Royal Society of Chemistry 2015

J. Mater. Chem. A, 2015, **3**, 13275–13282 | 13281

9 T. M. McCleskey, P. Shi and E. Bauer, *et.al.*, *Chem. Soc. Rev.*, 2014, **13**, 2141–2146.

10 V. F. Solovyov, T. Ozaki and A. Atrei, *et.al.*, *Sci. Rep.*, 2014, **4**, 4627.

11 C. H. Steele, *Solid State Ionics*, 2000, **129**, 95–110.

12 Y. Zhao, X.-F. Li and A. Khoryushin, *et.al.*, *Supercond. Sci. Technol.*, 2012, **25**, 015008.

13 Y. Zhao, W. Wu and X. Tang, *et.al.*, *CrystEngComm*, 2014, **16**, 4369–4372.

14 Y. Zhao, J.-C. Grivel and A. B. Abrahamsen, *et.al.*, *IEEE Trans. Appl. Supercond.*, 2011, **21**, 2912–2915.

15 Y. Zhao, J.-C. Grivel, M. Napari, D. Pavlopoulos, J. Bednarčík and M. von Zimmermann, *Thin Solid Films*, 2012, **520**, 1965–1972.

16 T. Aytug, M. Paranthaman and K. J. Leonard, *et.al.*, *J. Mater. Res.*, 2005, **20**, 2988–2996.

17 L. Molina, H. Tan and E. Biermans, *et.al.*, *Supercond. Sci. Technol.*, 2011, **14**, 065019.

18 R. B. Mos, T. Petrisor Jr and M. S. Gabor, *et.al.*, *Thin Solid Films*, 2013, **513**, 491–498.

19 W. Zhao, A. Norman and S. Phok, *et.al.*, *Phys. C*, 2008, **468**, 1092–1096.

20 N. Vyshnavi and I. V. Driessche, *Prog. Solid State Chem.*, 2012, **40**, 57–77.

21 Y. Zhao, J.-C. Grivel and M. Liu, *et.al.*, *CrystEngComm*, 2012, **14**, 3089–3095.

22 S. X. Ren, E. A. Kenik, K. B. Alexander and A. Goyal, *Microsc. Microanal.*, 1998, **4**, 15–22.

23 A. Goyal, S. X. Ren and E. D. Specht, *et.al.*, *Micron*, 1999, **30**, 463–478.

24 T. Taneda, M. Yoshizumi and T. Takahashi, *et.al.*, *IEEE Trans. Appl. Supercond.*, 2013, **23**, 6601005.

25 V. Matias, J. Hänisch, E. J. Rowley and K. Güth, *J. Mater. Res.*, 2009, **24**, 125–129.

26 V. Matias, B. J. Gibbons and J. Hanisch, *et.al.*, *IEEE Trans. Appl. Supercond.*, 2007, **17**, 3263–3265.

27 M. Coll, A. Pomar and T. Puig, *et.al.*, *Appl. Phys. Express*, 2008, **1**, 121701.

28 Y. Zhao and J.-C. Grivel, *CrystEngComm*, 2013, **15**, 3816–3823.

29 P. Norton, A. Goyal and J. D. Budai, *et.al.*, *Science*, 1996, **274**, 755–757.

30 H. Hojaji, S. Hu, A. Barkatt, D. D. Davis and A. N. Thorpe, *Phys. C*, 1992, **195**, 135–144.

31 M. Daeumling, J. M. Seuntjens and D. C. Larbalestier, *Nature*, 1990, **346**, 332–335.

32 H. Huhtinen, M. Irjala and P. Paturi, *et.al.*, *Phys. C*, 2012, **472**, 66–74.

33 D. T. Verebelyi, D. K. Christen and R. Feenstra, *Appl. Phys. Lett.*, 2000, **76**, 1755–1757.